Research Report

2004-34T

Design and Parameter Effect Analysis of Dual-Rotor, Radial-Flux, Toroidally-Wound, Permanent-Magnet Machines

R. Qu*, T. A. Lipo

*GE Global Research
Building EP, Room 110-B
One Research Circle
Niskayuna, NY 12309

University of Wisconsin-Madison
2557B Engineering Hall
1415 Engineering Drive
Madison, WI 53706

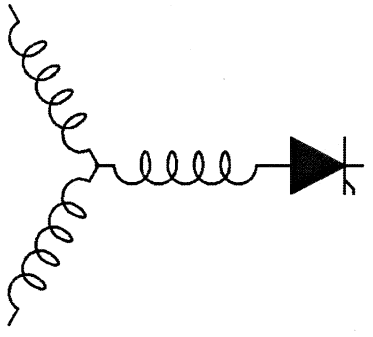

Wisconsin
Electric
Machines &
Power
Electronics
Consortium

University of Wisconsin-Madison
College of Engineering
Wisconsin Power Electronics Research Center
2559D Engineering Hall
1415 Engineering Drive
Madison WI 53706-1691

Design and Parameter Effect Analysis of Dual-Rotor, Radial-Flux, Toroidally Wound, Permanent-Magnet Machines

Ronghai Qu, *Member, IEEE,* and Thomas A. Lipo, *Fellow, IEEE*

***Abstract*—A novel machine family—the dual-rotor, radial-flux, toroidally wound, permanent-magnet (RFTPM) machine—has been proven in a previous paper to be able to improve the machine efficiency and boost the torque density. This paper will present the key design equations and design procedure of the RFTPM machines, analyze parameter effects on machine performance, and give design guidelines to achieve specific design objectives. In addition, finite-element analysis is employed to prove the effectiveness of the design equations and find the machine overload capability. Experimental measurements of a prototype, which match the design specifications well, verify the effectiveness of the design equations.**

***Index Terms*—Parameter effect analysis, permanent-magnet (PM) machine design, radial-flux, toroidally wound, permanent-magnet (RFTPM) machine.**

I. Introduction

HIGH TORQUE density and high efficiency are two of the most desirable features for an electrical machine. Improvement of these features has been one of the main aspects of research on the electric machines in the last several decades. In order to provide a solution to this problem, a novel machine class—the dual-rotor, radial-flux, toroidally wound, permanent-magnet (RFTPM) machine—was proposed in [1]. Its principle of operation, configurations, and features were discussed. Three low-cost techniques were proposed and proven to be valid to reduce the cogging torque. The high torque density of the RFTPM prototype was reported (0.004 32 N · m/cm^3 from the 3-hp RFTPM prototype versus 0.001 51 N · m/cm^3 for an induction motor (IM) and 0.001 94 N · m/cm^3 for a 5-hp interior PM (IPM) machine), while the efficiency is still kept high (0.871 for the RFTPM, 0.825 for the IM, and 0.88 for the IPM). The features of the dual-rotor RFTPM machines are summarized as the following:

- greatly shortened end windings;
- high ratio of diameter to length;
- high efficiency;
- high torque density;
- low material costs;
- low-cost techniques available to reduce cogging torque.

This paper will derive design equations and a design procedure for such slotted, surface-mounted, RFTPM machines shown in Fig. 1. The analysis of parameter effects on machine performance, such as efficiency, torque density, and material costs, will be included as well. Design guidelines will be given to achieve design objectives. In addition, finite-element analysis (FEA) is employed to prove the effectiveness of the design equations, find the machine overload capability, and verify if the machine can survive under the short-circuit fault. Finally, the proposed design method is used to design an actual prototype. The experimental measurements, which closely match the design specifications, verify the effectiveness of the design equations.

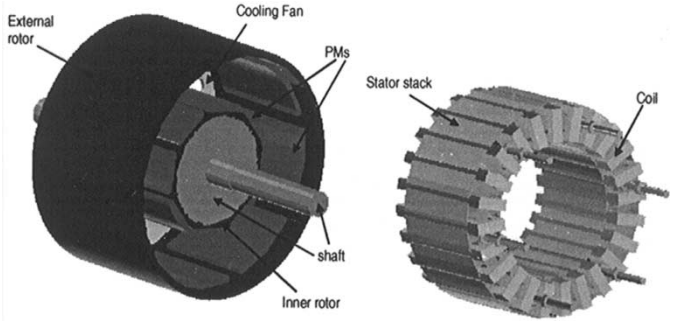

Fig. 1. Dual-rotor, toroidally wound, slotted, RFPM machine structure.

II. Design Equations

This section will give the key design equations for a dual-rotor, slotted, surface-mounted RFTPM machine shown in Fig. 1. The cross section is depicted in Fig. 2. Since this topology has two air gaps, the design equations are separated into two portions: one is for the internal portion of rotors, permanent magnets, and stator, and the other is for the external portion.

A. Fixed Parameters

Many unknown parameters are involved in the design of the RFTPM machines. As a result, it is necessary to assign some fixed values, and then determine the remaining as part of the design. The fixed parameters will be further explored in Sections V and VI based on a few different purposes. The fixed parameters

Paper IPCSD 04–002, presented at the 2003 Industry Applications Society Annual Meeting, Salt Lake City, UT, October 12–16, and approved for publication in the IEEE TRANSACTIONS ON INDUSTRY APPLICATIONS by the Electric Machines Committee of the IEEE Industry Applications Society. Manuscript submitted for review July 15, 2003 and released for publication January 24, 2004. This work was supported by the Wisconsin Electrical Machines and Power Electronics Consortium (WEMPEC).

R. Qu is with the GE Global Research Center, Niskayuna, NY 12309 USA (e-mail: qur@research.ge.com; ronghaiqu@ieee.org).

T. A. Lipo is with the Department of Electrical and Computer Engineering, University of Wisconsin, Madison, WI 53706 USA (e-mail: lipo@engr.wisc.edu).

Digital Object Identifier 10.1109/TIA.2004.827444

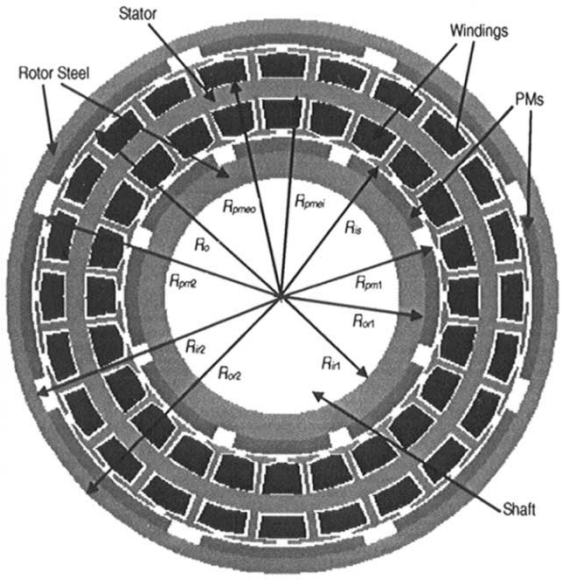

Fig. 2. Cross section of a dual-rotor, slotted, RFTPM machine.

TABLE I
FIXED PARAMETERS

No.	Parameters	Description
1	P_R or T	Power, W, or rated torque, N·m
2	N	Rated speed, rpm
3	N_c	Number of conductors in each slot
4	J_c	Current density, A/m^2
5	K_{s1}	Inner electrical loading, A/m
6	m	Number of phase
7	P	Number of poles for inner or outer magnets
8	q	Number of slots per phase per pole for inner or outer
9	C	Number of parallel circuits
10	g_1	Inner air gap length, m
11	g_2	Outer air gap length, m
12	L	Motor effective axial length, m
13	α_e ,α_m	Half electrical/mechanical angular width of each magnet, radian, refer to Fig. 3 and 4
14	B_r , μ_r	Magnet residual flux density, T, and recoil relative permeability
15	B_{g1} ,B_{g2}	Average flux densities of inner / outer air gap, T
16	B_{cr1} , B_{cr2}	Flux densities of inner / outer rotor core, T
17	B_{cs} ,B_{ts}	Flux densities of stator core / tooth, T
18	ρ	Conductor resistivity, ohm m^2/m
19	K_{cu}	Stator bare copper filling factor
20	K_{fw}	Loss factor of friction and windage
21	K_{fe}, ρ_{fe}	Lamination stacking factor and lamination mass density, kg/m^3
22	ρ_{steel}	Non-laminated steel mass density, kg/m^3
23	ρ_{cu}, ρ_{PM}	Material mass densities of copper and magnet, kg/m^3
24	N_{layer}	Number of layers per slot
25	τ_c	Coil pitch in slot pitch, $\tau_c \leq mq$

may vary depending on the design purpose. Table I gives a list of the fixed parameters used in the proposed design approach. They include machine power or torque, speed, machine winding information, electrical and magnetic loadings, etc.

B. Inner Portion Design

Assume initially that the inner radius of the inner air gap, $R_{\rm PM1}$, shown in Fig. 2 is known, which will be adjusted later to meet the power or torque requirement when the overall torque or power output is available. The inner magnet thickness, $H_{\rm PM1}$

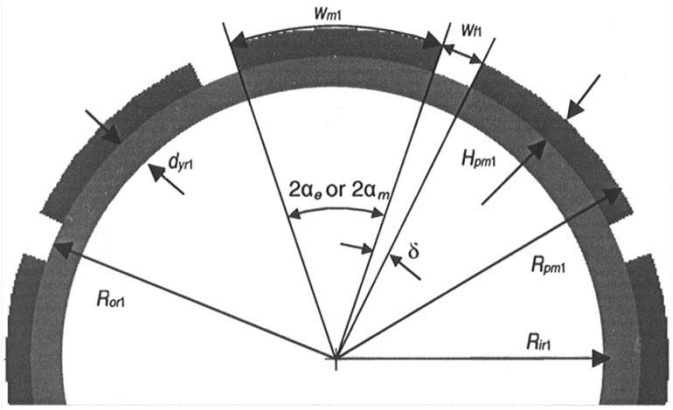

Fig. 3. Geometry of the inner rotor and magnets.

shown in Fig. 3, can be found from (1) [2], in which the air-gap leakage flux is considered

$$B_{g1} = \left[1 + \frac{w_{f1}}{w_{m1}} + \mu_r \frac{g_{e1}}{H_{\rm PM1}} \frac{w_{m1} + w_{f1}}{w_{m1} + 2g_{e1}} \times (1 + 2\eta_1 + 4\lambda_1)\right]^{-1} B_r \quad (1)$$

where w_{f1} is the circumferential length between two inner magnets, w_{m1} is the inner magnet circumferential length, g_{e1} is the effective inner air gap, and

$$\eta_1 = \frac{H_{\rm PM1}}{\pi \mu_r w_{m1}} \ln\left(1 + \frac{\pi g_{e1}}{H_{\rm PM1}}\right) \quad (2)$$

$$\lambda_1 = \frac{H_{\rm PM1}}{\pi \mu_r w_{m1}} \ln\left(1 + \frac{\pi g_{e1}}{w_{f1}}\right). \quad (3)$$

In (1), the only unknown is $H_{\rm PM1}$, which can be solved by iterative methods. The inner magnet working point B_{m1} can be calculated from the geometric parameters given above using (4) [2], [4]

$$B_{m1} = \frac{\left(1 + \frac{2g_{e1}}{w_{m1}}\right) \frac{1}{\mu_r} \frac{H_{\rm PM1}}{g_{e1}} + 2\eta_1 + 4\lambda_1}{\left(1 + \frac{2g_{e1}}{w_{m1}}\right) \frac{1}{\mu_r} \frac{H_{\rm PM1}}{g_{e1}} + 1 + 2\eta_1 + 4\lambda_1} B_r. \quad (4)$$

Then, the back-iron width d_{yr1} and the inner radius of the inner rotor or the shaft radius $R_{\rm ir1}$ can now be written as

$$d_{yr1} = \frac{w_{m1} B_{m1}}{2B_{cr1}} \quad (5)$$

and

$$R_{\rm ir1} = R_{\rm or1} - d_{yr1} \quad (6)$$

where the outer radius of the inner rotor $R_{\rm or1}$ is directly related to the inner radius of the inner air gap $R_{\rm PM1}$ by the magnet thickness.

The inner stator tooth width is given by

$$w_{ts1} = \frac{K_{Lt1} B_{g1} \tau_{s1}}{K_{fe} B_{ts}} \quad (7)$$

where K_{Lt1} is the inner air-gap leakage flux coefficient, which can be estimated using an analytical equation [2], [4] or from

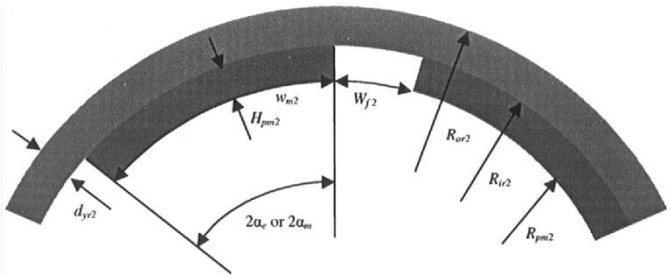

Fig. 4. Geometry of the outer rotor and magnets.

FEA results. Given the current density and electrical load are J_c and K_{s1}, respectively, the inner slot cross-sectional area available for conductors must be

$$A_{\text{slot1}} = \frac{2\pi R_{is} K_{s1}}{K_{cu} N_s J_c} = \frac{\beta R_{is} K_{s1}}{K_{cu} J_c} \tag{8}$$

where K_{cu} is the copper filling factor, N_s is the slot number, and β is the angular slot pitch in mechanical radians. The inner radius of the stator core is now easily found based the slot shape.

C. Outer Portion Design

The outer portion shares some common parameters with internal portion: the slot number N_s, current density J_c, and the slot area ($A_{\text{slot2}} = A_{\text{slot1}}$). To begin the outer design work, it is convenient to assume the outer radius of the outer air gap R_{PM2}, depicted in Fig. 4, is known. Then, the stator outer radius R_{os} is easily found from the given outside air gap g_2. Equations (1)–(3) can be used to find the outside magnet thickness, H_{PM2}, as well, by simply replacing the subscript 1 using 2, which stands for the outer rotor variables. Then, the inner radius of the outer rotor R_{ir2} is the sum of H_{PM2} and R_{PM2}.

Similar to (5), the outer rotor back-iron width is found to be

$$d_{yr2} = \frac{w_{m2} B_{m2}}{2 B_{cr2}}. \tag{9}$$

Then, the outer radius of the outer rotor R_{or2} must be

$$R_{\text{or2}} = R_{\text{ir2}} + d_{yr2}. \tag{10}$$

The designed stator core flux density is now ready to be calculated as

$$B_{cs} = \frac{K_{Lt1} K_{Ltt1} B_{g1} \tau_{p1} + K_{Lt2} K_{Ltt2} B_{g2} \tau_{p2}}{2 K_{fe} d_{ys}} \tag{11}$$

where d_{ys} is the stator yoke thickness, K_{Ltt1} and K_{Ltt2} are the factors of the leakage flux traveling from shoe to shoe, not through the back iron, for inner and outer air gaps, respectively, and $\tau_{p1,2}$ is the stator inner/outer pole pitch.

Equation (11) gives the calculated stator core flux density. The difference between the value of (11) and the desired one in Table I directs the designer to adjust the initial value of R_{PM2}, which forms the inner loop in the design flowchart shown in Fig. 5. Equations (1)–(11) describe the machine geometric sizes and flux distribution. Based on these parameters and keeping in mind that the inner windings are in series with the outside one, the machine power output, losses, efficiency, material volumes, and weights are easily found using the PM machine theory [3], [5], [6]. Therefore, those equations are omitted in this paper.

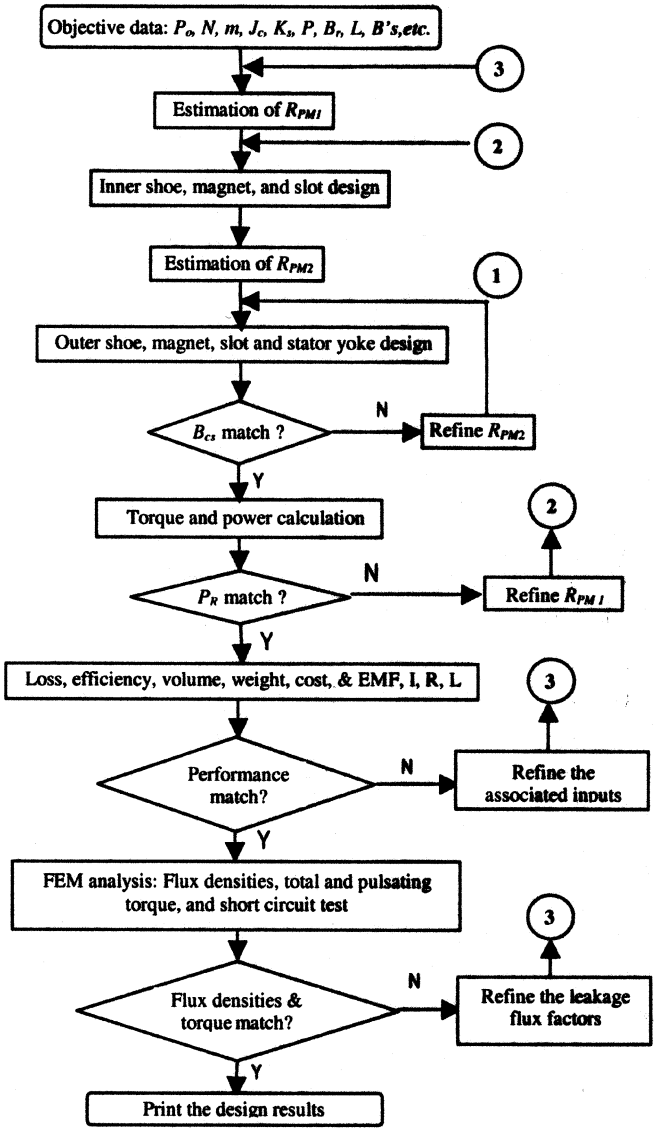

Fig. 5. Design flowchart.

III. Design Procedure and Flowchart

The design procedure and flowchart is shown in Fig. 5. The first step in designing a machine is to specify the input data needed in the process as per the design objective. After estimating the radius R_{PM1}, the equations in Section II-B can be evaluated. Once the outer part design is completed based on the estimation of R_{PM2}, the stator yoke flux density B_{cs} found using (11) has to be compared with the desired value. If they do not match each other well, the outer part design should be repeated based on the refined R_{PM2} until they match each other. According to the researcher's experience, this loop needs to run 2–4 times. Another loop is to make sure the power output matches the desired one by adjusting the radius R_{PM1}. Both loops can be automatically finished by a computer program. After that, back electromotive force (EMF), current, resistance, and inductance of the phase can be obtained and the performance of losses, efficiency, material volumes, and weights can be calculated.

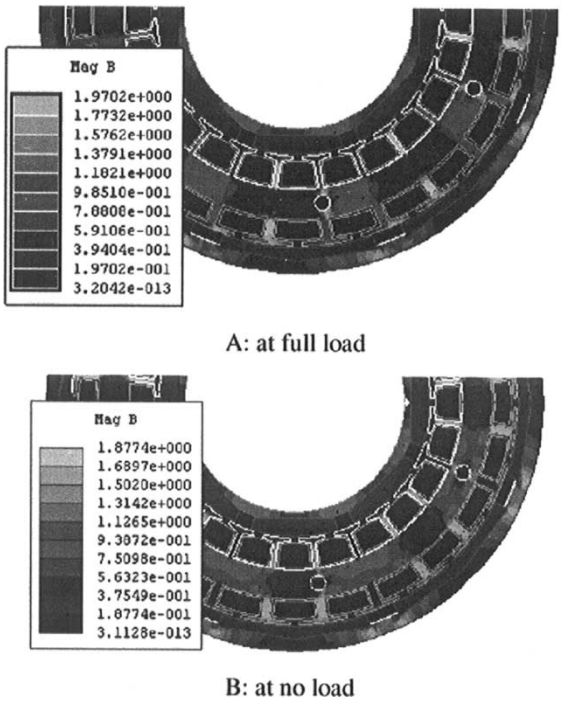

Fig. 6. Flux density distribution.

Usually, this completes the design of a machine. However, if the designer is not satisfied with the performance, the third loop will be formed by backing to the beginning with the necessary adjustment of the input data. In addition, finite-element method (FEM) analysis may be necessary to verify the analytical result, fine tune it, and build confidence. Based upon the FEM analysis, the leakage flux factors may need to be updated to calculate the flux distribution more accurately.

The motor designed by this procedure should be quite causational, but may not be the optimal one since the input data have the significant effect on the motor and they have not been analyzed. The input data to be analyzed include parameters such as the magnetic loading, electrical loading, and the main aspect ratio. This work will be done in Sections V and VI.

IV. FEAs

The FEA method is employed in this section to verify the effectiveness of the design equations, refine the leakage flux factors, find the machine overload capability, and verify if the machine can survive under the short-circuit fault.

A. Flux Distribution

Fig. 6 shows the flux distributions at full load and no load for a 3-hp slotted dual-rotor RFTPM motor with 0.7-mm air gaps. The design data are: 1800 r/min, eight poles, 120 Hz, efficiency 0.884, current density 551 A/cm^2, and inner/outer electrical loading 200/159 A/cm. The comparison shown in Table II demonstrates that all the design values well match the measurements except the stator core flux density, which is lower than the designed value by about 15%. This is mainly caused by the leakage flux in the screw holes punched on the stator lamination to fix the stator. The slot leakage flux, which has not been considered in the equations in Section II, also has a contribution to the flux density discrepancy. The inner magnets were designed to have the "loaf" shape to reduce the magnet manufacture cost. The armature reaction can be observed comparing Fig. 6(a) and (b) or from Table II, although it is as weak as expected.

TABLE II
COMPARISON OF THE DESIGNED AND FEA RESULTS

	Designed	FEA at full load	FEA at no load
B_{m1} (T)	0.262	0.2586 (ave.)	0.2609
B_{m2} (T)	0.255	0.2374 (ave.)	0.2489
B_{cr1} (T)	0.9	0.9417	0.8651
B_{cr2} (T)	1.65	1.768	1.64
B_{cs} (T)	1.7	1.64	1.46
B_{st1} (T)	1.6	1.81	1.658
B_{st2} (T)	1.6	1.783	1.569
Torque T (Nm)	12.73	13.09	

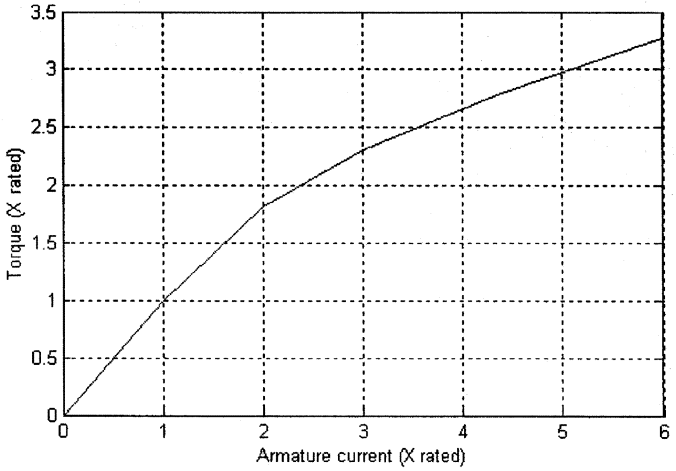

Fig. 7. Overload capability.

B. Overload Capability

Overload capability is another important machine parameter. Short-period overload capability is very desirable for some applications. The surface-mounted PM machines have high overload capability achieved by taking more current due to the low armature reaction. The torque associated with $2\times$ rated current is 23.87 N·m, which is $1.82\times$ the rated torque. When $3\times$ the rated current is fed, $2.31\times$ the rated torque will be produced. Fig. 7 demonstrates the torque variation with the armature current. It clearly shows the strong overload capability. The torque almost linearly increases as the current increases before it reaches $2\times$ the rated current.

C. Short-Circuit Protection

It is well known that PMs must be protected against reverse fields exceeding some value H_D. The magnet flux density must not be reduced below a certain value of B_D. Typically, the value of B_D is about -0.2 T at 100 °C for currently available Nd–Fe–B materials [6].

One of the main reasons to cause the magnet demagnetizing is the short-circuited current, which is usually a few times the rated armature current. The effect of the stator field on the magnet is to increase its flux density on the leading edge and decreases it

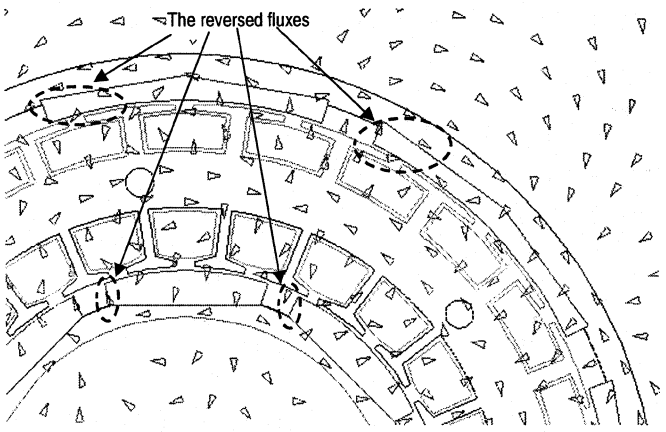

Fig. 8. B vector distribution in the motor cross-sectional area at the short-circuited current.

on the lagging edge. FEM analysis can simulate this situation by simply signing the short-circuited current to the windings.

Fig. 8 shows the B vector (the flux density) distribution in the motor cross-sectional area during a short circuit ($6\times$ the rated current). The four areas circled by black dashed lines are the areas where the fluxes are opposite to that driven by the magnets. The amplitudes of the reversed fluxes are smaller in the inner magnets (0.05 T) than those in the outer magnets (0.09 T) since the magnet thickness outside is a little smaller than the inside ones.

Compared with the B_D value – 0.2 T, the magnets still can survive from the short circuit with a little range of safety. If it is desired to increase the safety range, a longer air gap or a larger magnet can be a choice. It has also been found that the approach to increase the ratio of the leakage to magnetizing inductance is helpful [6].

V. Analyses of Parameter Effects on Machine Performance

This section will analyze the parameter effects on machine main performance based on the equations derived in Section II. Under an assumption that the leakage fluxes at both ends of the machine are negligible, some examples to show the parameter effects on machine performance will be demonstrated in this section.

A. Aspect Ratio and Pole Number

Figs. 9–12 show the effect of the pole number and the main aspect ratio K_{L1} of machine inner stator diameter D_{is} to length L_r on machine efficiency, torque density, material cost, and weight, respectively. The main machine parameters are: three phases, 3-hp, 1800 r/min, $\alpha_e = 75°$, $B_{m1} = 0.25$ T, $K_{s1} = 330$ A/cm, and $J_c = 448$ A/cm^2. Ferrite magnets are employed.

Figs. 9–12 illustrate that the aspect ratio is one of the main parameters to be optimized. Efficiency, torque density, material cost and weight are all strongly a function of the aspect ratio. For the example shown in these plots, an aspect ratio of 0.5–1.5 can achieve the best torque density with reasonable efficiency, material cost, and weight.

Also, note that the values of the aspect ratio for the maximum torque density vary slightly with the pole number. In addition,

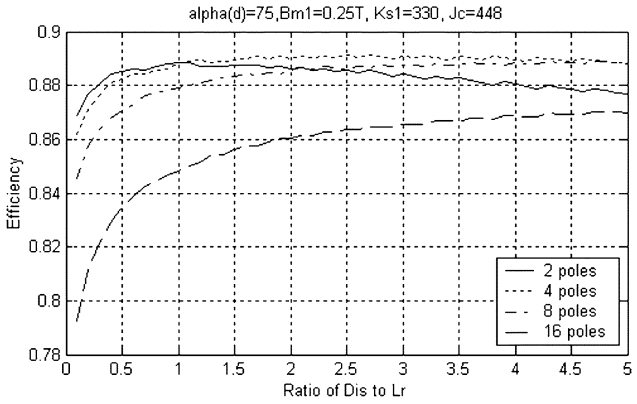

Fig. 9. Efficiency versus the ratio of D_{is} to L_r.

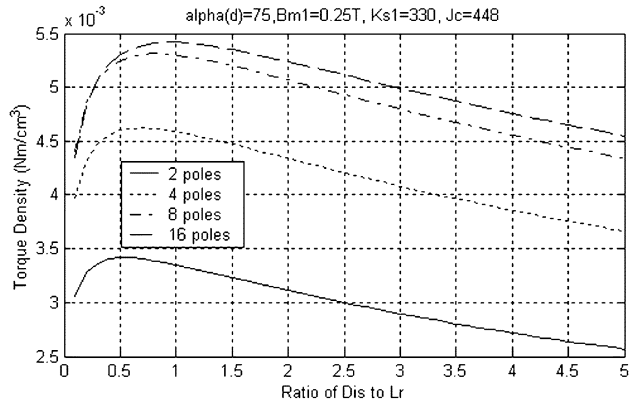

Fig. 10. Torque density versus the ratio of D_{is} to L_r.

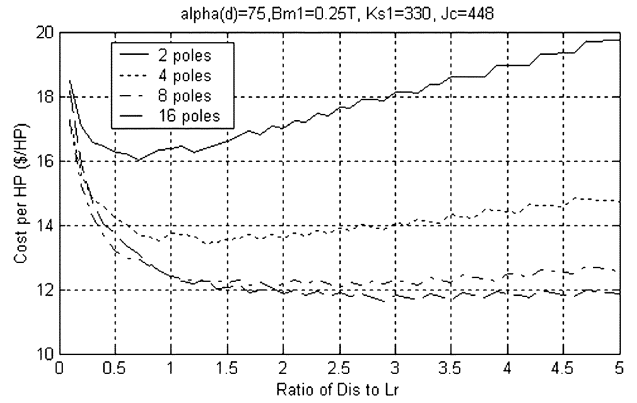

Fig. 11. Material cost per horsepower versus the ratio of D_{is} to L_r.

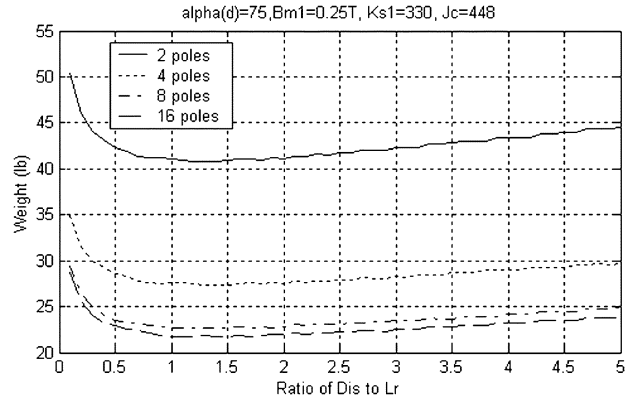

Fig. 12. Machine weight versus the ratio of D_{is} to L_r.

the curves may have different shapes for different speeds, magnetic loading, and electrical loading.

For the constant speed (1800 r/min for this case), the power supply frequency increases as the pole number increases, therefore, the iron losses increase as well and the efficiency decreases, which is shown in Fig. 9.

Fig. 10 shows that the torque density is enhanced by doubling the pole number, while the difference between two adjacent curves decreases as the pole number increases. This is the combined effects of the stator and rotor core thicknesses and the air-gap leakage flux. When the pole number is small, both stator and rotor cores are large and decrease quickly as the pole number increases, so that the machine torque density increases. When the pole number is large, however, the leakage flux increases faster and faster. Thus, the increase of the torque density becomes slower as the pole number increases. It can be foreseen that the torque density will decrease when the pole number is so high that the leakage flux effect is dominant.

The curves of the material cost and overall machine weight versus the aspect ratio of D_{is} to L_r are shown in Figs. 11 and 12. The ripples in these curves and in those in the following plots are caused by the discontinuity of the conductor number per slot.

B. Electrical Loading and Current Density

The electrical loading and current densities are important elements to be optimized in machine design. It is common knowledge that the torque density will increase as either electrical loading or current density increases, as shown in Fig. 14 for a constant-power machine. In addition, the material cost and the overall weight decrease as well. However, the efficiency depicted in Fig. 13 decreases as the penalty of electrical loading and current density increases. This implies that more cooling capability is required due to the higher power losses per unit air gap shown in Fig. 17. Thus, the design goal may become to achieve the highest torque density for a given efficiency η_o, or a pound number of the weight, etc. On the contrary, the goal may be to optimize the efficiency, weight, or material cost for a given torque density. In the curves in Figs. 13–17, eight poles and an aspect ratio of 1.3 were used based on Figs. 9–12.

The highest torque density can be obtained by selecting different points that have the same efficiency but on the different curves of electrical loading. For example, Points A, B, C, D, and E, shown in Fig. 13, on the five different curves of $K_{s1} = 264$, 297, 330, 363, and 396 A/cm, respectively, have the efficiency $\eta_o = 0.87$. However, point B has the highest torque density of all shown in Fig. 14. Point E can achieve the lowest material cost shown in Fig. 15 and the lowest power losses per unit air gap shown in Fig. 17, while point A possesses the lightest weight shown in Fig. 16. Which point to be selected is dependent upon the design purpose.

C. Magnetic Loading

The magnetic loading again plays a major role in PM machine designs. The selection of the magnetic loading still remains a task. The air-gap flux density and the angular width of each magnet $(2\alpha_e)$ may vary from motor to motor, and the resultant torque density, efficiency, and material cost also differ. Several plots cited in this section will demonstrate this influence. They are obtained using a ceramic magnet, one of the ferrites. The magnet residual flux density B_r is reduced to 0.322 from the original 0.4 T to represent the temperature effect.

Although the efficiency shown in Fig. 18 monotonously increses as the more magnet material is used, the torque density is not in the same situation. Fig. 19 shows that the highest torque density is achieved by the curve with B_{m1} of 0.25 T, not by

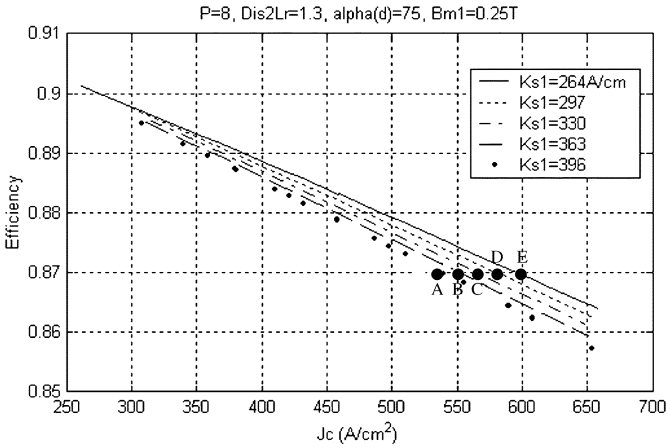

Fig. 13. Efficiency versus the electric load and current density.

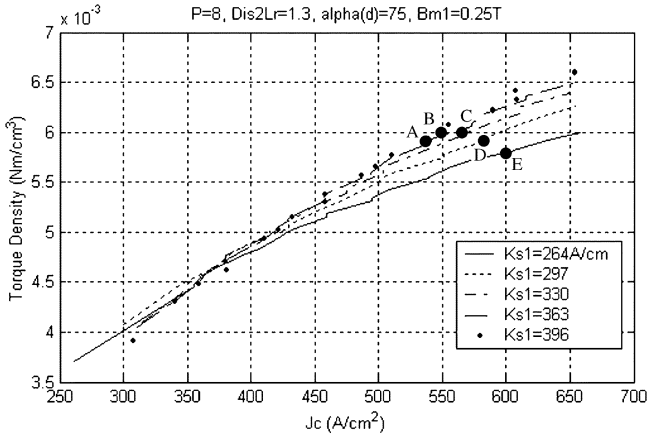

Fig. 14. Torque density versus the electric load and current density.

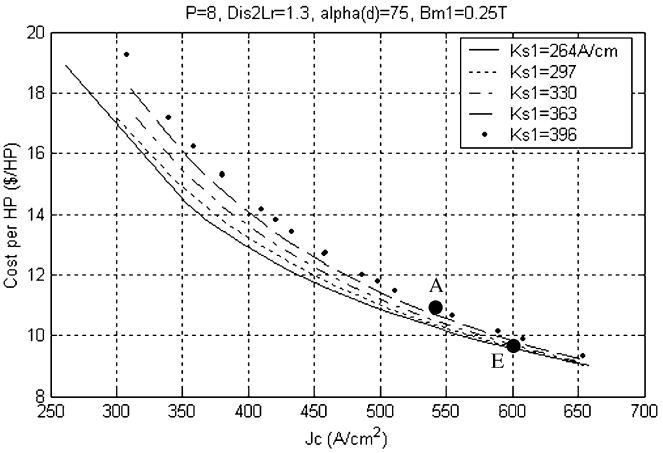

Fig. 15. Material cost versus the electric load and current density.

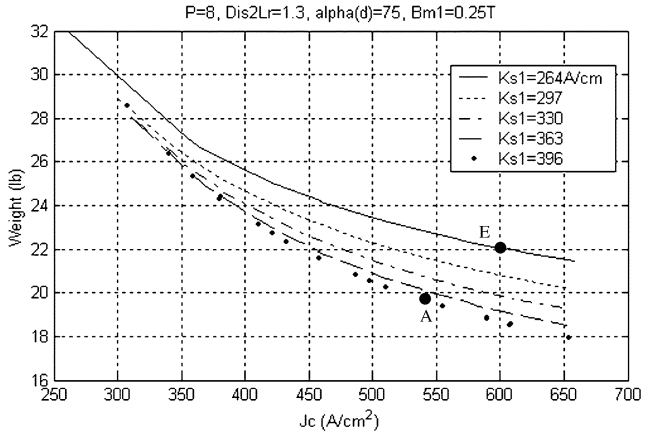

Fig. 16. Machine weight versus the electric load and current density.

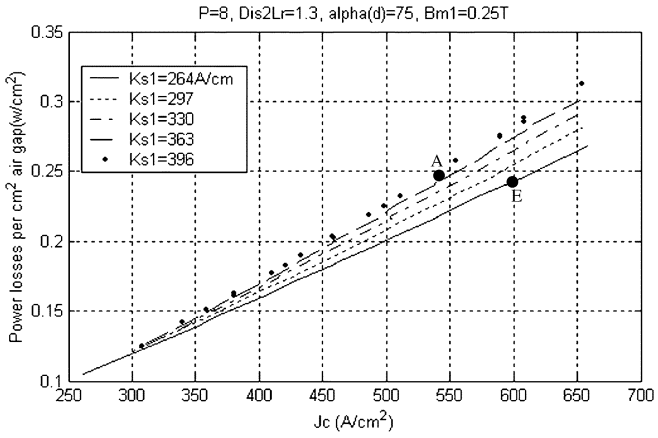

Fig. 17. Power losses per unit air gap versus the electric load and current density.

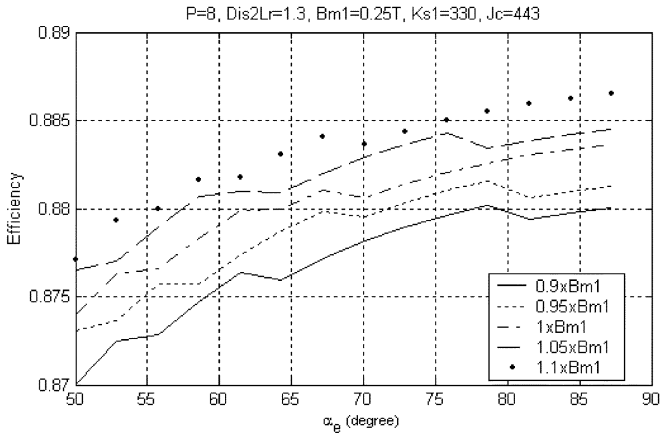

Fig. 18. Efficiency versus B_{m1} and α_e.

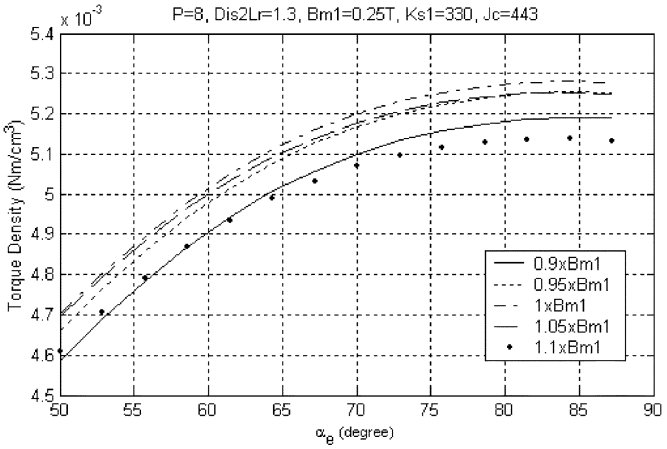

Fig. 19. Torque density versus B_{m1} and α_e.

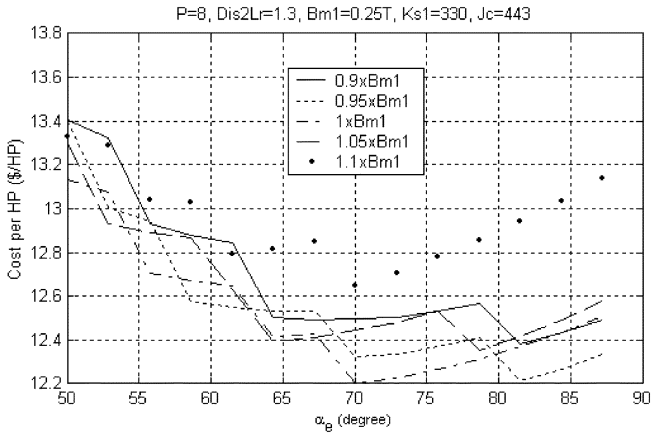

Fig. 20. Material cost per horsepower versus B_{m1} and α_e.

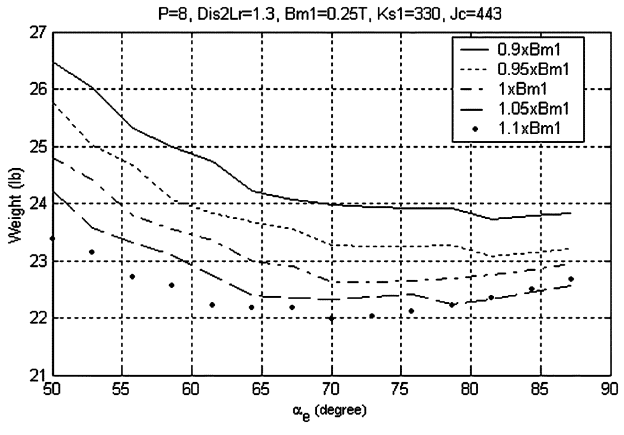

Fig. 21. Machine weight versus B_{m1} and α_e.

those with the flux densities having a scaling factor of 0.9, 0.95, 1.05, and 1.1. Meanwhile, the torque density increases with the magnet angle α_e. When α_e is close to 90°, the magnet-to-magnet leakage flux increases quickly so that the increasing torque density slows. For $B_{m1} = 0.25$ T, the lowest material cost per horsepower shown in Fig. 20 and the lighest weight in Fig. 21 are achieved when α_e is approximately 70°–75°. It also has been noted that to obtain the maximum torque density, the magnet working point (flux density) are slightly different for the inner and outer magnets.

D. Design Guideline

To consider the six variables discussed in this section in the design process, a design guideline is proposed and shown in Fig. 22. It is helpful to note that the different design processes may be needed to achieve the different design purposes.

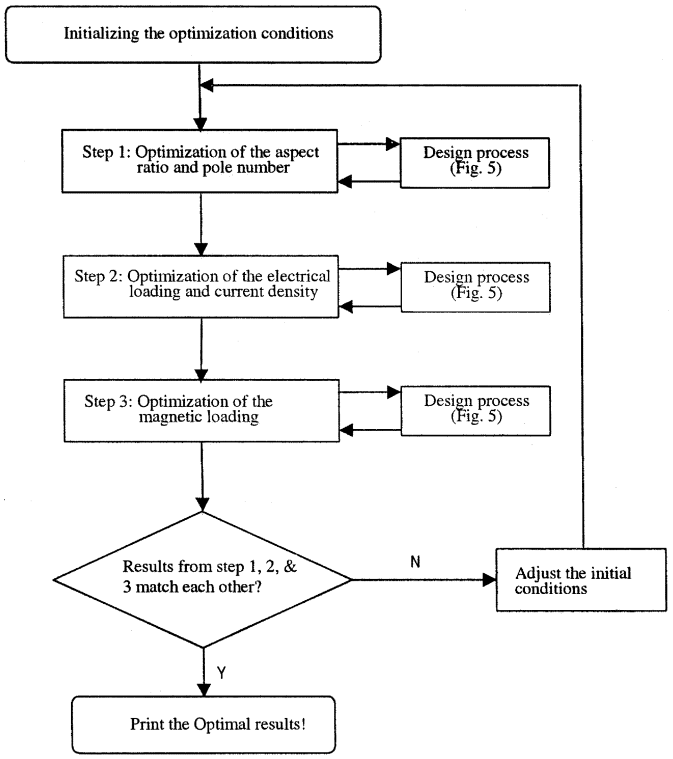

Fig. 22. Design flowchart including the effects of the aspect ratio, pole number, electric, and magnetic loadings.

In each design step shown in Fig. 22, the design flowchart in Fig. 5 has to be run several times to reach the optimal point. The results from the previous step should be used as the next step initial conditions. The results of the last step usually do not match the initially assumed conditions used in the first step. Thus, this design process has to be repeated with the updated initials until all the optimal results from each step well match the initial conditions of the others.

VI. Prototype Design and Experimental Results

An RFTPM prototype motor was designed using the derived equations and the design guidelines with the following ratings, in which the dc-bus voltage and phase current were selected to be suitable for 600-V 25-A insulated gate bipolar transistors (IGBTs):

power	3 hp;
torque	11.87 N·m;
speed	1800 r/min;
efficiency	87%;
dc-bus voltage	380 V;
trapezoidal phase current	9.1 A, peak.

The main design objective is to achieve the maximum torque density while keeping 87% efficiency.

Given the tradeoff study in Section V-A, eight poles and an aspect ratio of 1.3 were selected for the prototype. Concentrated, full-pitch, single-layer, toroidal windings distributing in 24 slots were employed. To keep the material cost low, ceramic magnets (also known as ferrite) are used. The residual flux density B_r is 0.4 T and the temperature coefficient of B_r is -0.20 %/°C. In order to lower the labor cost, the magnets are designed with parallel sides rather than strict arc segments, while the inner magnets have a "loaf" shape, as shown in Fig. 23(a).

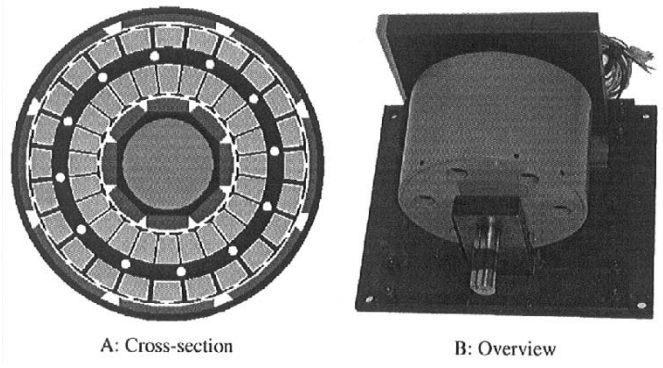

Fig. 23. Dual-rotor RFTPM prototype.

TABLE III
Main Physical Sizes of the Prototype (Unit: Centimeters)

R_{or2} = 8.852	R_{ir2} = 8.436	R_{PM2} = 8.020	R_{os} = 7.930
R_{is} = 4.392	R_{PM1} = 4.332	R_{or1} = 3.916	R_{ir1} = 3.150
d_{ys} = 0.982	L_r = 6.757	g_1 = 0.060	g_2 = 0.090

Following the design procedure and guidelines shown in Figs. 5 and 22, the electric and magnetic parameters were set to

$$\begin{aligned} K_{s1} &= 245\ \text{A/cm} \\ K_{s2} &= 186\ \text{A/cm} \\ Jc &= 452\ \text{A/cm}^2 \\ \alpha_{e1} &= 75^\circ \\ \alpha_{e2} &= 80^\circ \\ B_{m1} &= 0.250\ \text{T} \\ B_{m2} &= 0.246\ \text{T} \\ B_{g1} &= 0.208\ \text{T} \\ B_{g2} &= 0.225\ \text{T}. \end{aligned}$$

The main machine physical sizes are summarized in Table III.

The measured prototype output torque and efficiency are 12.65 N·m and 89.8% when the machine is cold and 11.78 N·m and 87.1% at the steady state, respectively. Both the steady-state values well match the design ones. These results prove the validity of the derived design equations and the proposed design procedure. More experimental results for the steady state are summarized as follows [1], [4]:

speed	1800 r/min;
output torque	11.78 N·m;
phase current	7.15 A, rms;
mechanical loss	66 W;
efficiency	87.1%;
output power	2.98 hp;
copper loss	238 W;
other losses	24 W.

VII. Conclusion

The key design equations and procedure of the RFTPM machines have been presented. Analyses of parameter effects on machine performance have been made. In addition, some design guidelines to achieve the design objectives were given. The FEA

results and the prototype measurements verify the effectiveness of the design equations and procedure.

REFERENCES

[1] R. Qu and T. A. Lipo, "Dual-rotor, radial-flux, toroidally-wound, permanent-magnet machines," in *Conf. Rec. IEEE-IAS Annu. Meeting*, vol. 2, Pittsburgh, PA, Oct. 2002, pp. 1281–1288.

[2] ——, "Analysis and modeling of airgap & zigzag leakage fluxes in a surface-mounted-PM machine," in *Conf. Rec. IEEE-IAS Annu. Meeting*, vol. 4, Pittsburgh, PA, Oct. 2002, pp. 2507–2513.

[3] D. C. Hanselman, *Brushless Permanent-Magnet Motor Design*. New York: McGraw-Hill, 1994.

[4] R. Qu, "Design and analysis of dual-rotor, radial-flux, toroidally-wound, surface-mounted-PM machines," Ph.D. dissertation, Dept. Elect. Comput. Eng., Univ. Wisconsin, Madison, WI, 2002.

[5] J. R. Hendershot Jr and T. J. E. Miller, *Design of Brushless Permanent-Magnet Motor*. Oxford, U.K.: Magna Physics/Clarendon, 1994.

[6] T. A. Lipo, *Introduction to AC Machine Design*. Madison, WI: Wisconsin Power Electronics Research Center, Univ. of Wisconsin, 1998, vol. 2.

Ronghai Qu (S'01–M'02) is a native of China. He received the B.E.E. and M.S.E.E. degrees from Tsinghua University, Beijing, China, in 1993 and 1996, respectively, and the Ph.D. degree in electrical engineering from the University of Wisconsin, Madison, in 2002.

From 1996 to 1998, he was a faculty member of the Electrical Engineering Department, Tsinghua University, and in 1998, he joined the Wisconsin Electric Machines and Power Electronics Consortium (WEMPEC) as a Research Assistant. He became a Senior Electrical Engineer at Northland, a Scott Fetzer Company, in 2002, and in 2003, he joined the GE Global Research Center, Niskayuna, NY, where he is presently an Electrical Engineer in the Electric Machines and Drives Laboratory. He has authored 13 published technical papers and has two U.S. patents pending and several disclosures.

Dr. Qu received the President Jiang Nanxiang Award from Tsinghua University in 1992. He received the Third Prize Paper Award from the Electric Machines Committee of the IEEE Industry Applications Society (IAS) for presentations at the 2002 IAS Annual Meeting. He is a Member of Sigma Xi.

Thomas A. Lipo (M'64-SM'71-F'87) was born in Milwaukee, WI. He received the B.E.E. and M.S.E.E. degrees from Marquette University, Milwaukee, WI, in 1962 and 1964, respectively, and the Ph.D. degree in electrical engineering from the University of Wisconsin, Madison, in 1968.

From 1969 to 1979, he was an Electrical Engineer in the Power Electronics Laboratory of Cooperate Research and Development of the General Electric Company, Schenectady, NY. He became a Professor of Electrical Engineering at Purdue University, West Lafayette, IN, in 1979, and in 1981, he joined the University of Wisconsin, Madison, in the same capacity, where he is presently the W. W. Grainger Professor for Power Electronics and Electrical Machines, Co-Director of the Wisconsin Electric Machines and Power Electronics Consortium, and Director of the Wisconsin Power Electronics Research Center. He has authored 400+ published technical papers and is the holder of 32 U.S. patents.

Dr. Lipo has received the 1986 Outstanding Achievement Award from the IEEE Industry Applications Society (IAS), the 1990 William E. Newell Award of the IEEE Power Electronics Society, and the 1995 Nicola Tesla IEEE Field Award from the IEEE Power Engineering Society for his work. He has served the IEEE in various capacities for three IEEE Societies, including President of the IAS. He is a Fellow of the Institution of Electrical Engineers, U.K., and the Royal Academy of Engineering (Great Britain), and a Member of the Institute of Electrical Engineers of Japan. He has received 21 IEEE Prize Paper Awards from three different IEEE Societies including Best Paper Awards for publication in the IEEE TRANSACTIONS in the years 1984, 1994, and 1999.